

STATIC GROUND EFFECT OF HIGH-ASPECT-RATIO WINGS

Chen Zheng[1], Qiulin Qu[2], Peiqing Liu[3], Tianxiang Hu[4]

[1,2,3,4]Beihang University, Beijing, 100191, People's Republic of China

Abstract

Static ground effect exerts a remarkable impact on the aerodynamic performance of high-aspect-ratio wings. At present, relevant research is mostly limited to rectangular wings, and the ground effect mechanisms of swept wings have not been fully understood. This paper conducts numerical investigations on high-aspect-ratio rectangular and swept wings under static ground effect, and analyzes the flow characteristics from the forward flight perspective. The results show that the flow fields of the two wing types follow the same rule, formed by the superposition of flow components normal and parallel to the leading edge. The influence of wingtip flow is confined to a fixed spanwise range and fails to affect the inboard region, where two-dimensional flow governs. The ground boundary restrains streamline deflection and divergence to sustain such two-dimensional flow, and the bound vortex strength declines as airflow escapes from the wingtip. The conclusions presented here can offer physical insights for the aerodynamic analysis and design of high-aspect-ratio wings operating near the ground.

Keywords: ground effect, high aspect ratio, aerodynamic forces, wingtip vortex

1. Introduction

High-aspect-ratio swept wings have long been a mainstream configuration widely adopted in civil airliners and military transport aircraft to suppress induced drag and improve cruise aerodynamic efficiency, while emerging ultra-high-aspect-ratio wing designs have been extensively applied to long-endurance unmanned aerial vehicles (UAVs). Moreover, innovative configurations represented by the Transonic Truss-Braced Wing (TTBW) [1-2] are considered a promising technical pathway for next-generation civil aircraft, further highlighting the engineering value of high-efficiency swept wing layouts. Takeoff and landing are the most accident-prone stages, where ground effect (GE) is a critical factor. Differing from unbounded free-stream flow conditions, ground proximity significantly distorts the near-body flow field and alters aerodynamic performances, and this influence is defined as the GE. For widely applied high-aspect-ratio swept wing aircraft, it is particularly essential to clarify the underlying GE mechanisms during low-altitude flight.

According to dominant flow mechanisms, ground effect can be classified into chordwise-dominated GE for two-dimensional airfoils and spanwise-dominated GE for three-dimensional finite wings. For a certain flight height h, the former is governed by the height-to-chord ratio h/c (where c denotes the mean aerodynamic chord), whereas the latter is characterized by the height-to-span ratio h/b (where b represents the wing span). Notably, at the same flight height, wings with a larger aspect ratio (AR) produce a considerably stronger spanwise-dominated GE. When the aircraft's flight height remains constant, the influence of the ground is defined as the static ground effect (SGE), which typically occurs during the aircraft's taxiing phase. The vast majority of existing literature on GE concentrates on SGE.

The chordwise-dominated SGE represents the most well-established area of research on GE. According to existing experimental and numerical studies [3-7], within the most common range of

https://doi.org/10.71945/icas2026_0295

small-to-moderate angles of attack (AOA), GE leads to an increase in the pressure on both the upper and lower surfaces of the airfoil, which can be attributed to the camber reduction effect and the blockage effect, respectively. At large flight heights, the pressure increment on the upper surface is more significant, resulting in a decrease in lift; the opposite trend is observed at small flight heights.

A portion of research on spanwise-dominated SGE has focused on the behavior of wingtip vortices. The primary observed phenomena [8-11] are as follows: In the vertical direction, the wingtip vortices first descend to the ground and then rebound downstream, which is due to the formation and induction of the secondary vortex; In the spanwise direction, the wingtip vortices move outwards due to the mirror-image effect from the ground. Another branch [12-15] of research has concentrated on predicting the aerodynamic forces of wings under GE. In GE research, the mirror vortex model [16] has been widely adopted as a mainstream approach for equivalent flow field simulation. This method treats the ground as a symmetry plane to mirror the actual flow field, whereby the ground effect is equivalently represented by the induced effect of mirror vortices. Previous studies generally employ the Prandtl lifting-line theory with mirror vortex corrections to predict aerodynamic coefficients under GE, which delivers satisfactory accuracy for rectangular wings. Current investigations into spanwise-dominated GE have predominantly been conducted on rectangular wings, while no relevant systematic studies on swept wings have been found in the available literature.

In fact, accurate aerodynamic modeling of swept wings is challenging even under unbounded free-flow conditions without ground interference. The conventional lifting-line theory is inherently inapplicable to swept wings. Although several modified lifting-line methods [17-18] have been proposed for swept wing corrections, their formulations are essentially close to the panel method, lacking the simplicity of classical analytical theories. More importantly, the complex flow characteristics of swept wings near the symmetry plane cannot be accurately reproduced by conventional physical models, rendering high-precision aerodynamic prediction for swept wings extremely challenging under both unbounded flow and GE conditions. In this context, exploring the underlying flow physics of swept wings in these complex GE flow environments becomes far more essential. It can provide fundamental physical insights and reliable theoretical support for the aerodynamic design of wings and airfoils, filling the research gap in this field.

In this paper, numerical studies are conducted on simple high-aspect-ratio rectangular wings and swept wings, with the primary focus on the spanwise distribution of aerodynamic forces and the corresponding flow mechanisms.

2. Physical Model and Numerical Method

2.1 Physical model

In this paper, the wings with AR = 6, 9, 15, ∞ and swept angle Λ = 0°-40°, are constructed with the NACA 4412 airfoil profile, as shown in Figure 1, where the origin of wind coordinate systems OXYZ is located at the leading edge. The chord length of c = 1m is chosen, and the semispan b/2 varies according to AR. The flight height h is defined as the vertical distance from the airfoil trailing edge to the ground. To facilitate comparisons with two-dimensional flow, the geometric pitch angle (α) is set to a consistent 6°for all wing sections, thereby ensuring a uniform flight height h. It should be noted that the α defined herein differs from the conventional AOA for the entire wing.

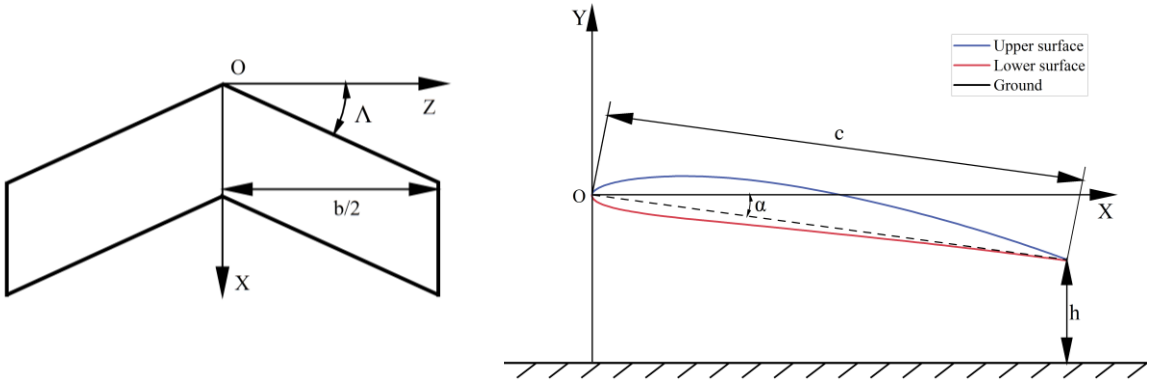


Figure 1 – Top view and cross-section of the swept wing.

The background pressure is set to 101,325 Pa in accordance with the International Civil Aviation Organization (ICAO) sea-level standard atmosphere. The free-stream Mach number of 0.2 and incoming flow velocity U_∞ = 68 m/s are adopted as the designated operating conditions, which is equivalent to 132 KTAS and corresponds to a Reynolds number Re = 4.66×10^6. The computational domain and boundary conditions are illustrated in Figure 2, where the half model is used to save the computational cost. Following the principle of relative motion, the light-yellow wing is kept stationary. The gray surfaces are set as the velocity inlet boundary with the velocity U_∞, the blue ground is set as the no-slip moving wall boundary with the velocity U_∞, and the red surface is set as the pressure outlet boundary with p_∞ = 101,325 Pa.

For a rectangular wing with a swept angle of 0°, the two-dimensional airfoil case corresponds to an infinite AR condition. For wings with a non-zero sweep angle, the left and right boundaries of the computational mesh are located at the two ends of the wing segment, where periodic boundary conditions are imposed to simulate the infinite AR state.

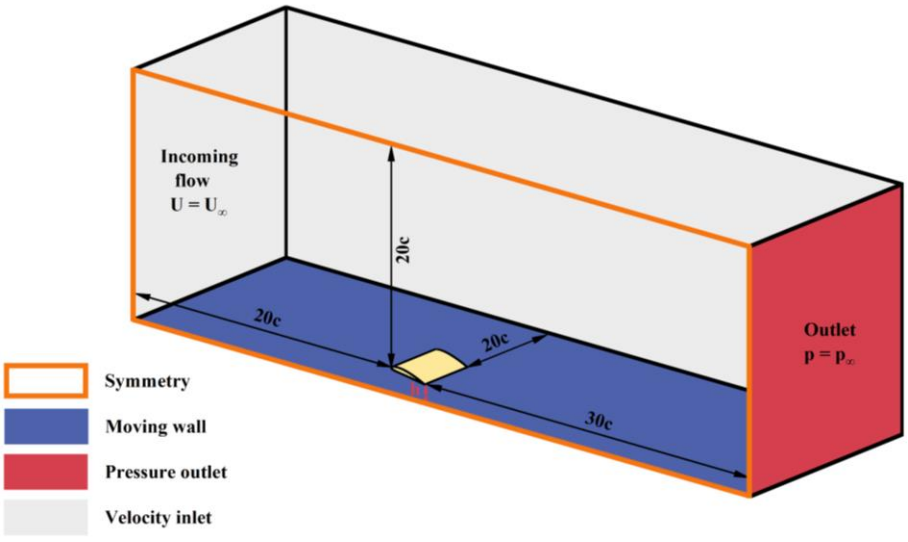


Figure 2 – Computational domain and the boundary conditions.

2.2 Numerical method

For the simulation, the double precision solver of ANSYS Fluent 2021R1 is utilized to solve the incompressible Reynolds-Averaged Navier-Stokes (RANS) equations with the SST k-omega turbulence model using the finite volume method (FVM). The pressure-based solver, which employs the semi-implicit method for pressure-linked equations consistent (SIMPLEC) algorithm, is used to handle the pressure-velocity coupling. The second-order central differencing scheme is applied to discretize the diffusion terms, while the second-order upwind scheme is used for the convection terms. To discretize time terms, the first-order implicit method is applied. Gradient reconstruction is performed using the least-squares cell-based gradient method. Flux reconstruction adopts the default total variation diminishing (TVD) slope limiter, with the cell-to-face limiting scheme enabled and the limiter filter disabled.

The SGE case of a rectangular wing with AR = 9 at flight height h/c = 0.2 is chosen to perform the mesh independence study. Coarse, medium and fine meshes are generated, and the first layer cell height in the three grids is maintained at approximately y+ = 1.0. Figure 3 shows the medium mesh on the wing surface, ground and symmetry plane. The computational results in Table 1 indicate that the aerodynamic force coefficients exhibit minimal variation among the three meshes. To balance the computational cost and accuracy, the medium mesh is chosen for the subsequent studies.

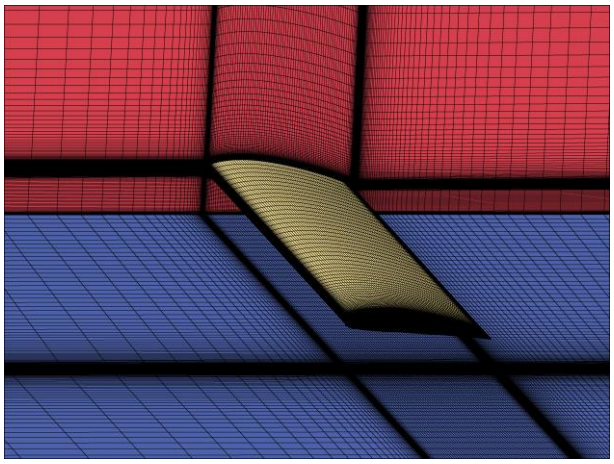


Figure 3– Medium mesh layout on wing surface, ground and symmetrical plane.

Table 1 – Assessment of mesh independence.

Mesh	Cell numbers	C_L	C_D
Coarse	7,789,304	1.03438	0.02218
Medium	15,913,350	1.03541	0.02211
Fine	34,493,502	1.03547	0.02211

2.3 Validation

The accuracy of the above numerical method in predicting the chordwise-dominated SGE and spanwise-dominated SGE is assessed respectively.

For the chordwise-dominated SGE, the inverted Tyrrell-026 airfoil with chord length c = 0.2234 m is chosen. The simulation conditions are: AOA = 3.6°h/ c = 0.224 (here h is defined as the vertical distance from the lowest point of airfoil to the ground), and Re = 4.6×10^5 based on the chord length, corresponding to the experimental conditions [19]. As illustrated in Figure 4, the pressure distributions predicted by the current CFD exhibit strong agreement with the experimental data.

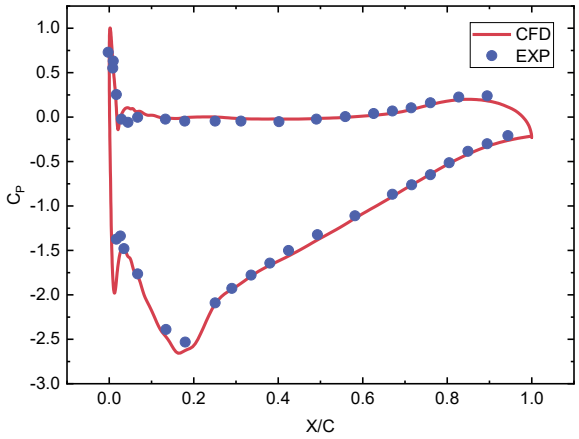


Figure 4 – Pressure distributions on the inversed Tyrrell-026 airfoil.

For the spanwise-dominated SGE, a rectangular wing based on the NACA 0012 airfoil with AR = 3.64 and c = 0.2794 m is chosen. The simulation conditions are: AOA = 10° U_∞ = 15 m/s, Re = 2.71×10^5 based on the chord length, and the flight height ranges from h/c = 1.0 to h/c = 0.05, corresponding to the experiment in Ref. [11]. To replicate the experimental conditions, the computational domain dimensions were set to match those of the wind tunnel. The static ground plane length was 5c, and a half-model configuration was employed, as illustrated in Figure 5. In general, the present CFD results reasonably reproduce the overall trend of the lift curve varying with flight height, as shown in Figure 6, with the absolute deviation of lift coefficient kept within 0.05. Furthermore, the wingtip vortex core position at x/c = 2.5, extracted from the CFD data (Figure 7), achieves a reasonable agreement with the experimental data obtained from the provided contours. For convenience, the coordinate systems used are identical to those in Ref. [11], where the origin is located at the wingtip leading edge, with the positive Z-axis directed from the wingtip toward the wing root, and the positive Y-axis oriented vertically upward.

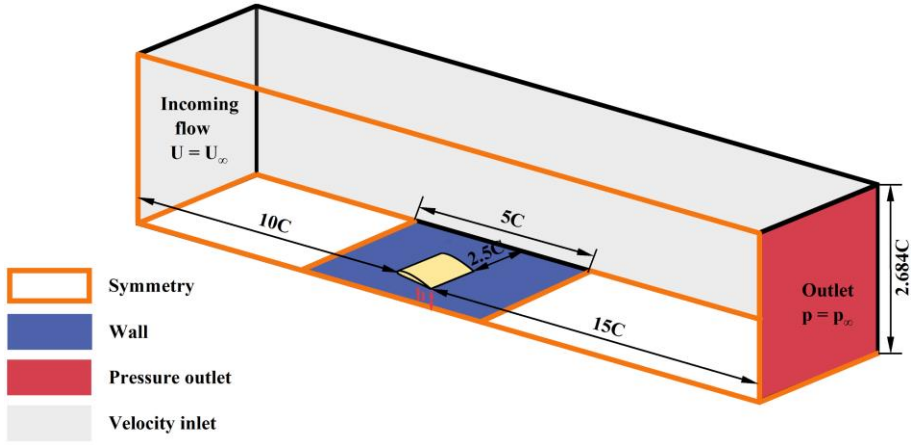


Figure 5 – Computational domain and the boundary conditions for the SGE validation case of wing.

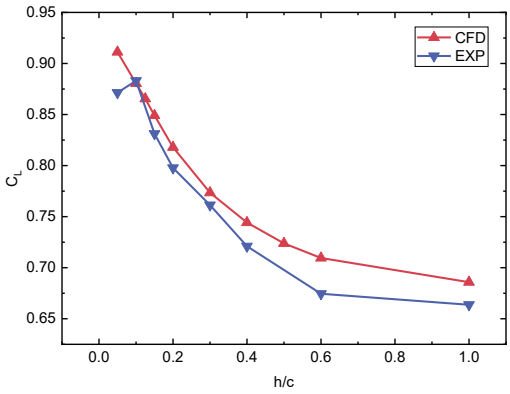


Figure 6 – Lift curve with flight height for the SGE validation case of wing.

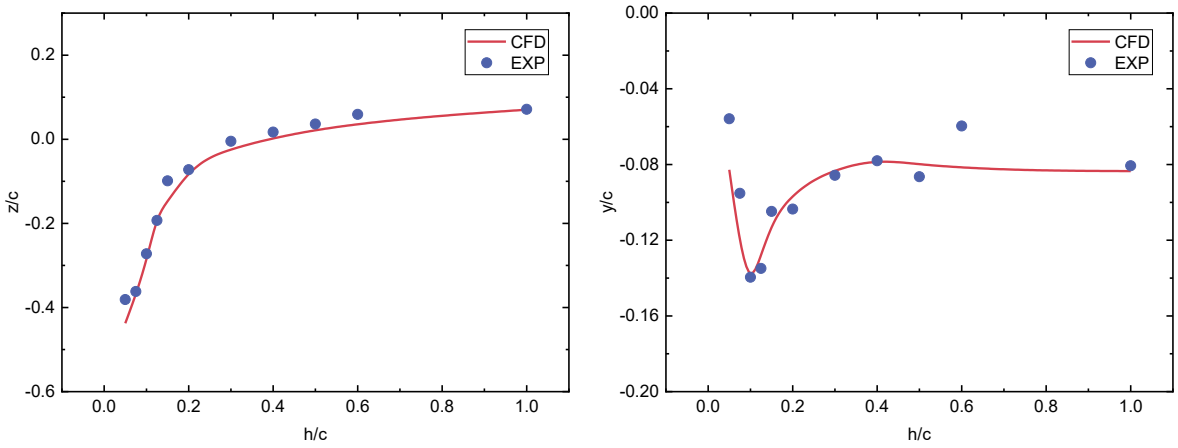
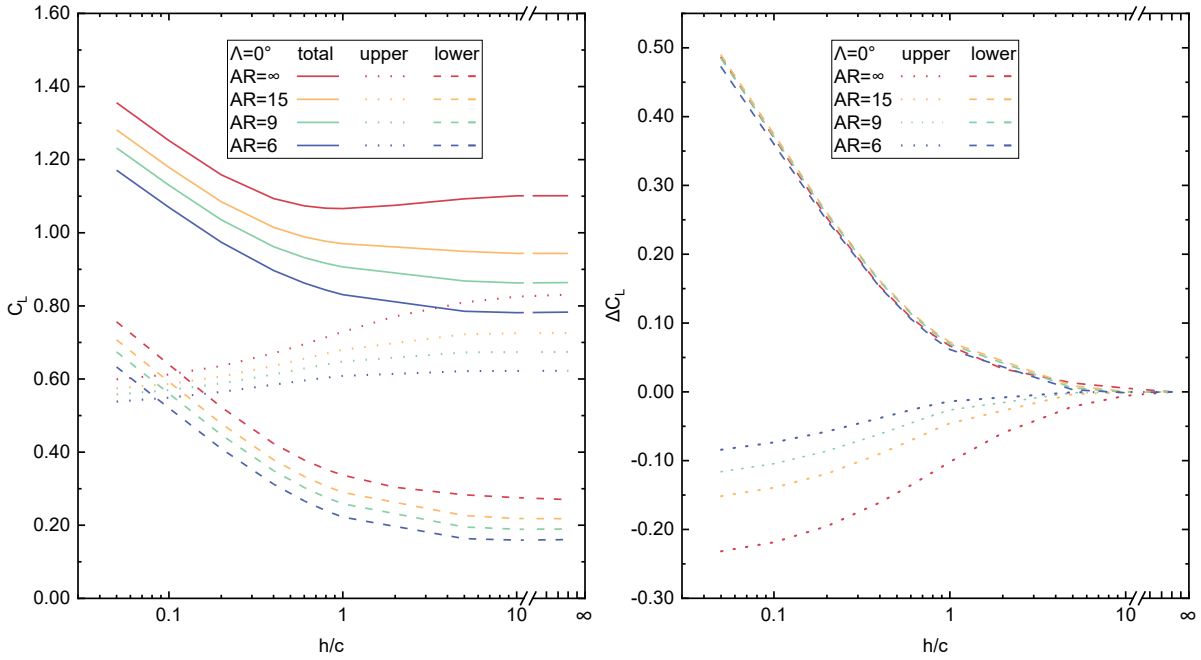


Figure 7 – The wingtip vortex core position at x/c = 2.5 with flight height for the SGE validation case of wing. (The coordinate systems used are identical to those in Ref. [11])

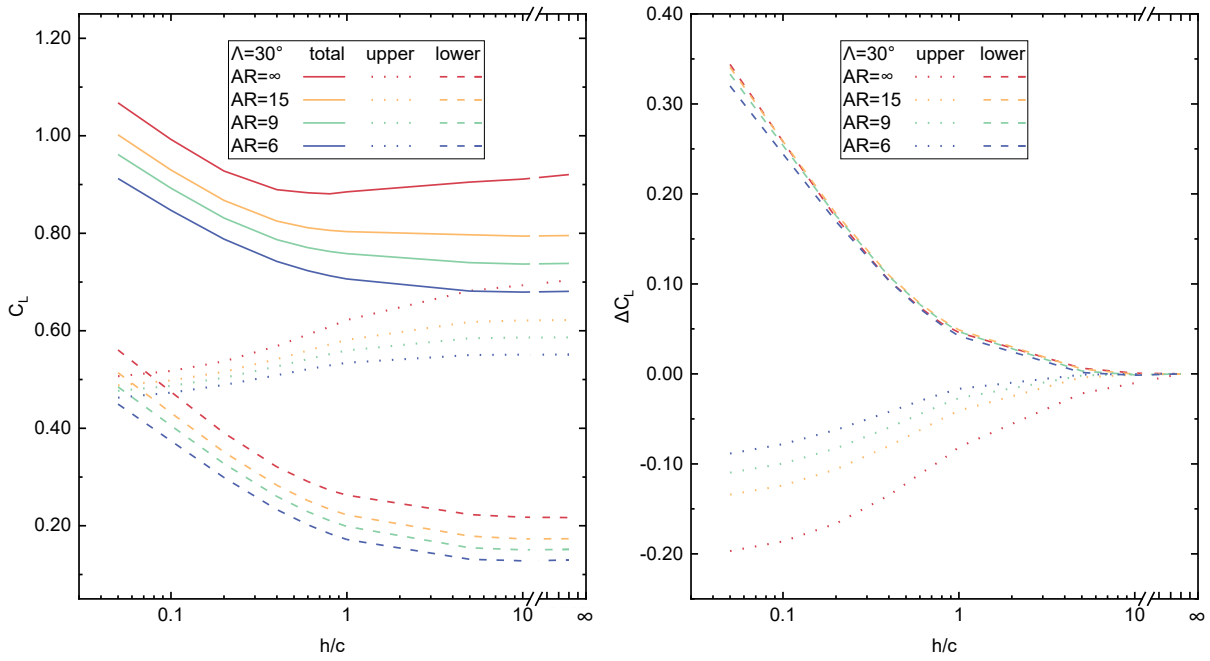
3. Results

3.1 Force coefficient characteristics

For the swept wing configuration, force coefficients are not calculated based on the area of the wing segment. Owing to the disparate effects on the upper and lower wing surfaces, force coefficient characteristics under GE are analyzed separately. For convenience, the subscripts up and $lower$ are employed to denote the upper and lower surfaces, respectively. For instance, $C_{L,up}$ refers to the local lift coefficient of the upper surface. The lift coefficients and their differences relative to h/c = ∞ are presented in Figure 8, where Figure 8(a) corresponds to the rectangular wing with a sweep angle of 0°and Figure 8(b) corresponds to the wing with a sweep angle of 30° Overall, the two types of wings exhibit consistent variation trends in lift coefficients. For both configurations, the lift on the upper surface decreases while the lift on the lower surface increases, resulting in an enhancement in the total lift. Notably, the variation in lower-surface lift demonstrates a surprisingly consistent tendency for wings with different AR.



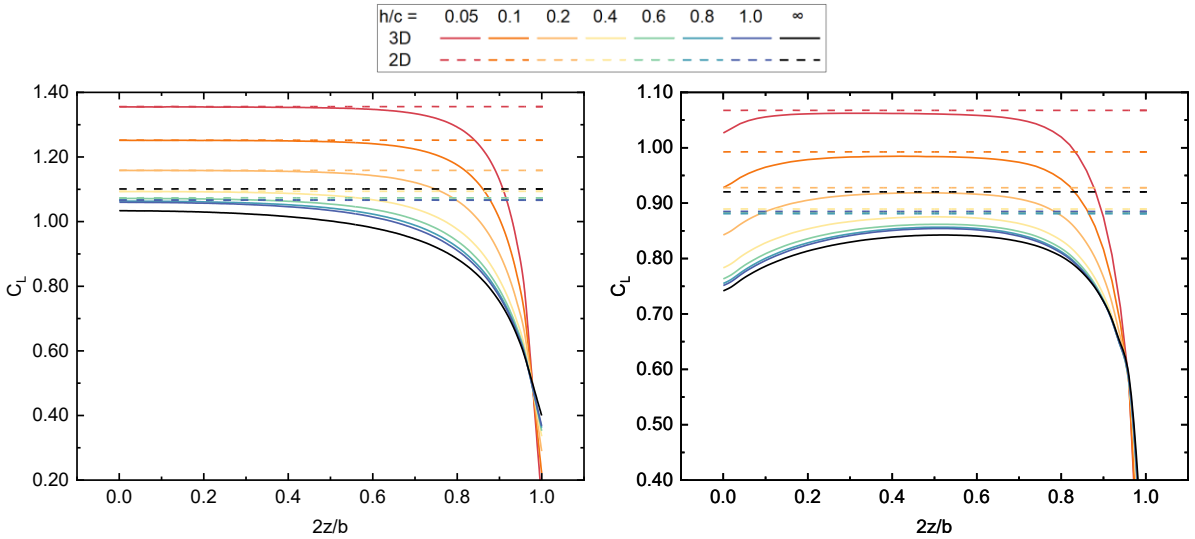
(a) Swept angle = 0° wings



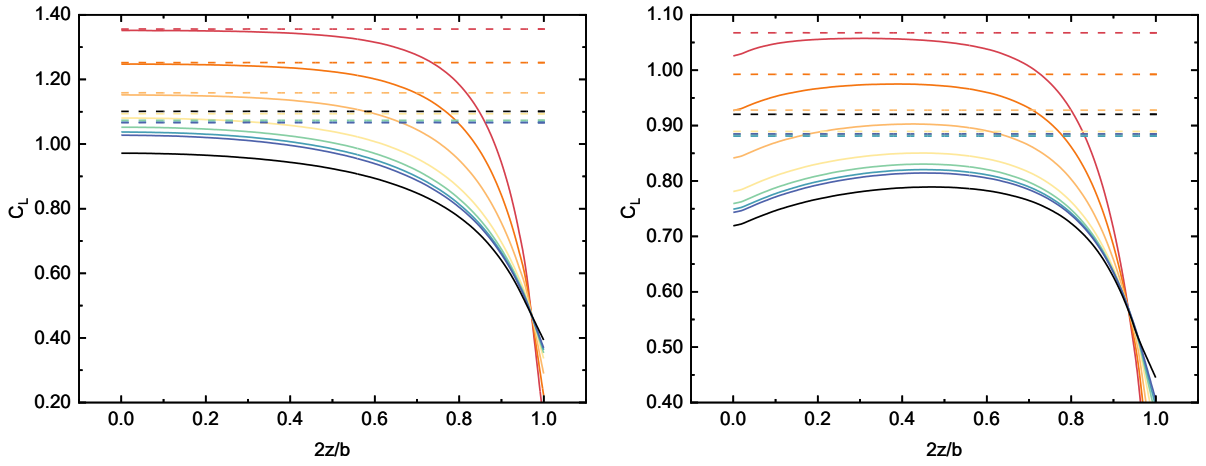
(b) Swept angle = 30° wings

Figure 8 – Lift coefficients (left) and their differences (right) relative to h/c = ∞.

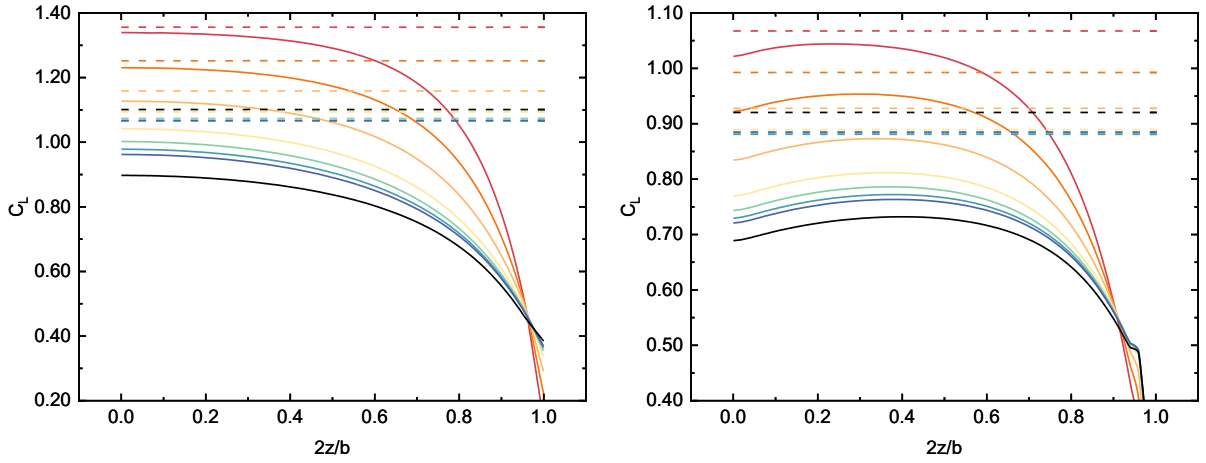
To further investigate the characteristics of force coefficients, the spanwise distributions of force coefficients are plotted. Figure 9 presents the spanwise distribution of C_L for rectangular wings (left) and 30° swept wings (right) at different flight heights, and their corresponding two-dimensional (2D) C_L. The 2D C_L presented herein corresponds to the lift coefficient of infinite AR wings. For the rectangular wing of AR = 15, in an unbounded flow field (h/c = ∞), the three-dimensional (3D) C_L distribution deviates significantly from 2D C_L. Conventionally, such discrepancies are attributed to downwash flow, which intensifies progressively from the wing root to the wing tip. When the wing is in proximity to the ground (h/c = 1.0), the C_L at the symmetry plane (2z/b = 0) is already in close agreement with 2D C_L. With a further reduction in flight height, the region on the inner wing where the 3D C_L coincides with 2D value expands gradually, accounting for approximately half of the wingspan at h/c = 0.05; this region is named as 2D flow region. For the swept wing of AR=15, apart from the reduction in C_L near the wing root, the mid-span segment of the wing also exhibits characteristics similar to those of 2D flow region at small flight heights. As AR decreases, the coverage of such 2D flow regions gradually diminishes. For the wing of AR = 6, no evident 2D flow region is formed even at an extremely low flight height of h/c = 0.05.



(a) AR = 15 wings



(b) AR = 9 wings



(c) AR = 6 wings

Figure 9 – Spanwise distribution of C_L for rectangular wings (left) and 30°swept wing s (right) at different flight heights, and their corresponding 2D C_L.

Overall, at small flight heights, excluding the end regions affected by the wing tip and the symmetry plane of swept wings, the lift on the remaining portion of the wing is consistent with that in the two-dimensional case. The flow characteristics in the wingtip region and mainstream region of the two wings are compared respectively, and the formation mechanism of 2D flow region is subsequently discussed.

3.2 Flow consistency near the wing tip

The geometric scale of wingtip vortices near the wing remains relatively fixed in different h/c. Given that the inboard wing section is unaffected by wingtip vortices, the spatial extent of their influence is theoretically invariant. Based on this assumption, the surface pressure distributions of rectangular wings with different aspect ratios are presented in Figure 10, where the wingtips of all configurations are aligned for intuitive comparison. The results show identical pressure distributions in the wingtip region across all cases. The wing with an aspect ratio of 15 essentially features an extended two-dimensional flow region while retaining consistent tip flow characteristics. This phenomenon is physically reasonable. Since the wingtip influence fails to propagate into the inboard two-dimensional flow region, arbitrary sectional boundaries selected within the inboard region do not alter the flow field near the wingtip.

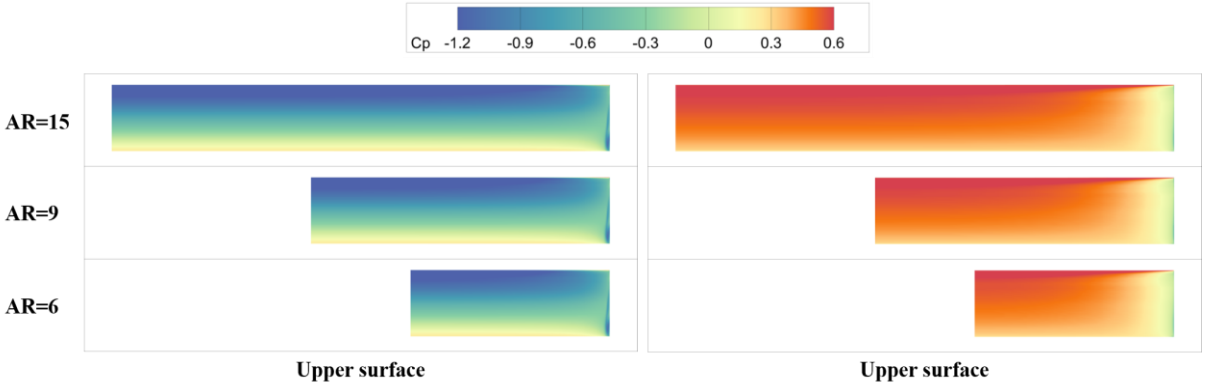


Figure 10 – Surface pressure distributions of rectangular wings with different AR at h/c = 0.2.

To compare the aerodynamic forces near the wingtips of wings with different AR, the maximum AR of 15 is selected as the anchor point for coordinate transformation. First, all the wings are aligned along their wingtips, followed by non-dimensionalization using the span length of the AR = 15 wing:

$$\frac{2z^*}{b} = \frac{2z + (15 - AR * c) * \cos\Lambda}{15c * \cos\Lambda} \tag{1}$$

Figure 11 presents the spanwise distribution of C_L for rectangular wings with different AR at h/c = ∞ (left) and h/c = 0.2 (right). For the unbounded flow field corresponding to h/c = ∞, the C_L of wings with different ARs exhibit convergence only at the wingtips. In contrast, under GE condition of h/c = 0.2, the C_L of wings with AR greater than 6 overlap completely across an extensive inboard region extending from the wingtips—this region corresponds approximately to the 0.7–1.0 spanwise segment of the AR =15 wing. A similar phenomenon can also be observed in the C_L distribution of swept wings, as shown in Figure 12. Subsequent studies will be dedicated to investigating the formation mechanism of the wingtip flow consistency.

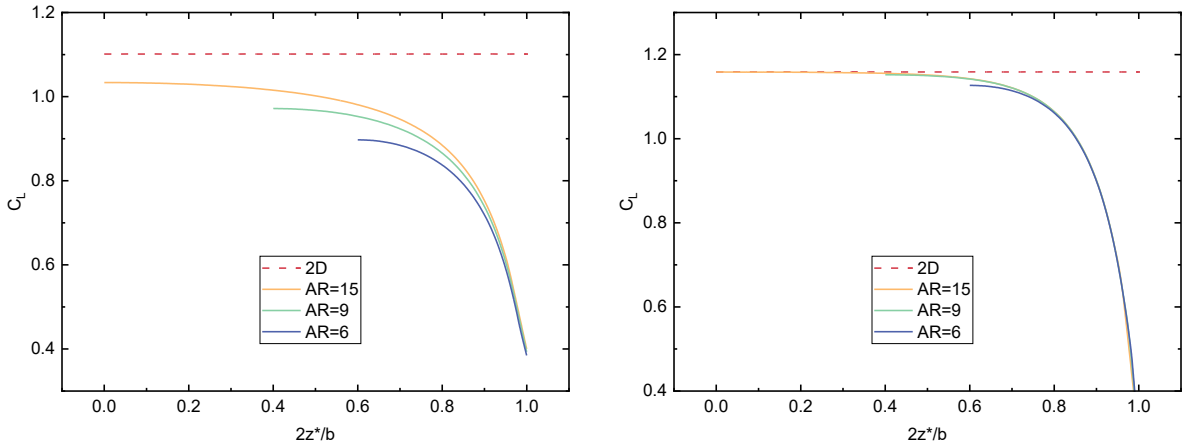


Figure 11 – Spanwise distribution of C_L for a rectangular wing with different AR at h/c = ∞ (left) and h/c = 0.2 (right).

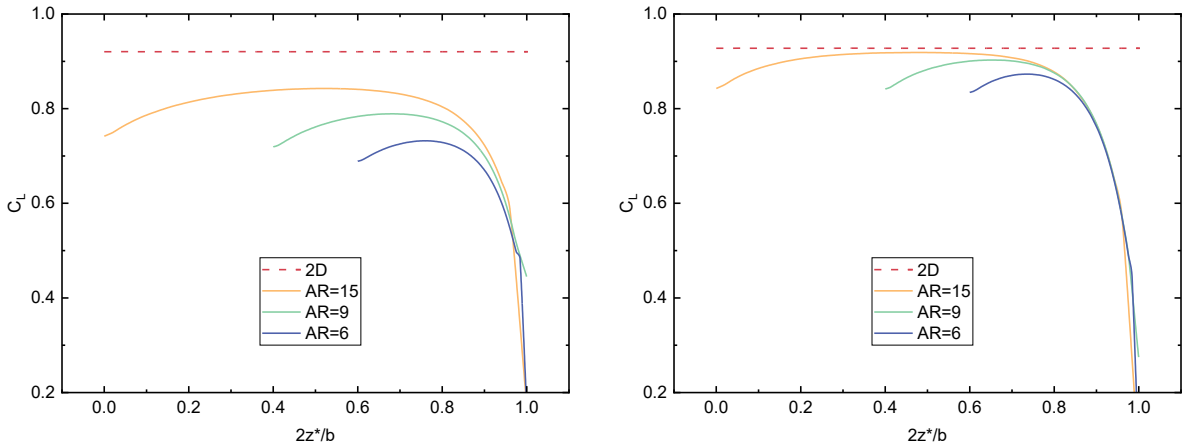


Figure 12 – Spanwise distribution of C_L for a 30° swept wing with different AR at h/c = ∞ (left) and h/c = 0.2 (right).

3.3 Flow field of mainstream region

Based on the foregoing discussion, the flow fields over rectangular and swept wings under GE can be generally divided into the wingtip influenced region and 2D flow region. For swept wings, lift is slightly reduced at the wing root due to the boundary effect of the symmetry plane, while the lift distribution in the remaining spanwise regions is highly similar with that of rectangular wings. On this basis, the consistency of flow structures between the two wing types is further discussed.

Conventionally, the incoming flow is decomposed into two components parallel and perpendicular to the leading edge to investigate the aerodynamic characteristics of swept wings. However, the mainstream flow and surface friction streamlines observed in experiments are generally parallel to the free stream, which fails to directly verify the rationality and variation characteristics of the conventional velocity decomposition method for swept wings. To address this issue, this study restores the physical perspective of the real wing flow field, namely the scenario of a forward-moving wing in a quiescent far-field atmosphere. Correspondingly, a new velocity field is obtained by subtracting the free-stream velocity from the original CFD calculation results:

$$\boldsymbol{U}' = \boldsymbol{U} - \boldsymbol{U}_\infty \tag{2}$$

Figure 13 illustrates the near-field streamlines around the NACA4412 airfoil and the far-field streamlines in the newly defined velocity field. As the airfoil moves forward, it pushes the airflow on its lower surface upstream; the airflow subsequently travels around the leading edge to the upper surface. The flow field attached to the airfoil corresponds to the classical attached vortex. In the far field, the effect of the attached vortex can be approximated as that of a point vortex, and the induced streamlines are nearly circular, with only slight deviations near the shear layer of the wake.

It is noteworthy that the flow around a two-dimensional airfoil exhibits a typical closed-streamline characteristic. The streamline initiating from the trailing edge on the airfoil lower surface consistently connects to the trailing edge on the upper surface, forming a closed flow streamline. This feature is more clearly demonstrated in the subsequent analysis, and numerical results at different angles of attack validate the physical regularity. For conciseness and logical coherence, detailed verifications are not presented herein.

From the perspective of flow mechanism, a failure of smooth connection of streamlines at the trailing edge would induce a two-dimensional spiral flow structure. As a fundamental property of potential flow, the two-dimensional irrotational spiral flow strictly relies on source-sink singularities, which are constructed by the superposition of a point source and a point vortex, as illustrated in Figure 14. In contrast, the ideal inviscid airfoil flow is a strictly divergence-free and source-free flow field without any source or sink components, which fundamentally suppresses the formation of spiral streamlines. Accordingly, the streamline enclosing all attached vorticity of the airfoil must be closed.

Under the inviscid potential flow assumption, the flow velocity magnitude and direction on the upper and lower surfaces at the trailing edge are identical. Combined with the incoming free-stream flow, this velocity consistency satisfies the classical Kutta condition.

To validate the classical Kutta-Joukowski lift circulation theory, equation (2) for an airfoil, the circulation is calculated by integrating along the closed streamlines surrounding the airfoil, and the corresponding lift coefficient is further converted. It is worth noting that the flow velocity rapidly decays to zero in the far field, where numerical errors in CFD simulations become prominent. The far-field streamlines exhibit multi-loop overlap, and the present circulation results are obtained based on the averaged single-loop integration.

$$L = \rho U_\infty \Gamma \tag{3}$$

In this study, the lift coefficient calculated via surface integration of the airfoil is 1.10. The lift coefficient converted from the circulation of the closed streamlines near the trailing edge is 1.20, while those obtained from two sets of far-field streamlines both equal 1.15. Discrepancies in the lift-circulation theorem originate primarily from wake shear effects, though the overall prediction accuracy remains satisfactory. The uniform free stream contributes zero circulation to the closed integral path, indicating that the circulation magnitude is independent of the forward-flight frame transformation. Overall, the forward-flight perspective adopted in this study is more physically intuitive.

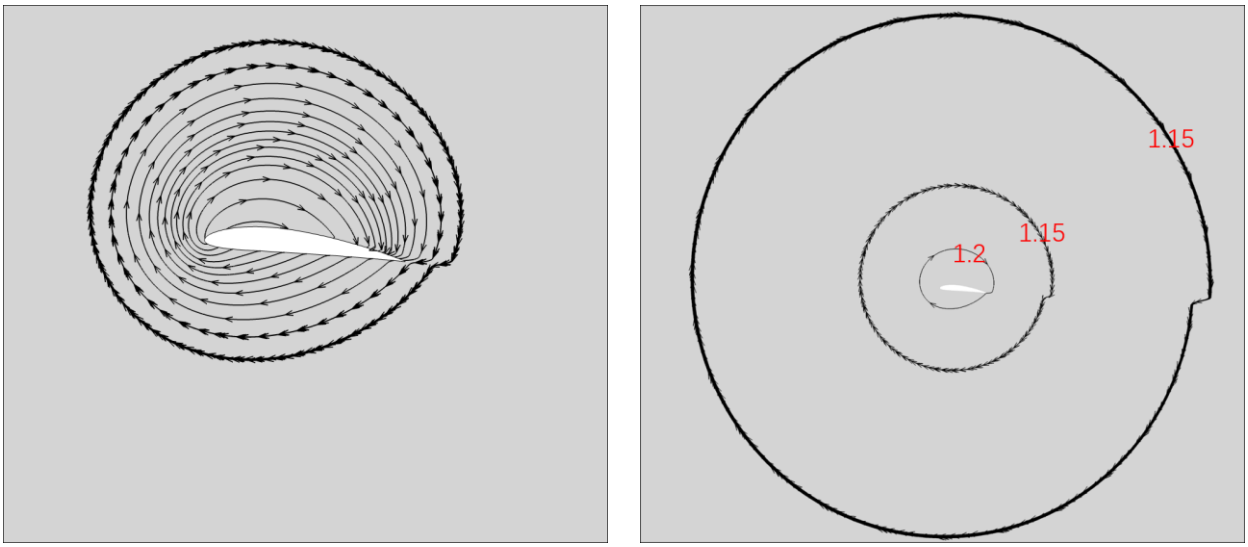


Figure 13 – Near-field streamlines (left) around the NACA 4412 airfoil and the far-field streamlines (right) under the forward flight frame.

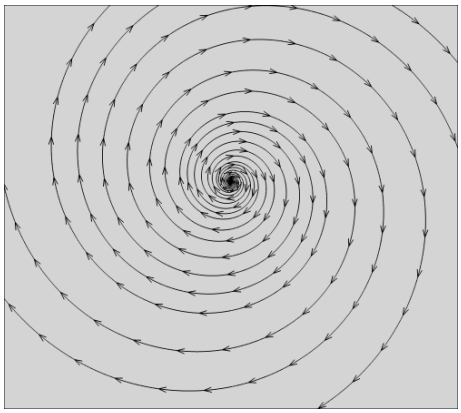


Figure 14 – Streamlines of superposed point source and point vortex.

For clearer visualization, several sampling points around the airfoil are selected, as shown in Figure 15. Streamlines passing through these points on the upper surface are extracted to characterize the local flow, and the same approach is applied to the lower surface. To avoid visual clutter, not all streamlines across the sampling points are plotted.

Figure 16 presents the flow features on the upper and lower surfaces of the rectangular wing with AR =15 at relative flight heights of h/c = ∞ and h/c = 0.05, while Figure 17 shows the corresponding results for the 30°swept wing with the same AR. It is observed that the flow is predominantly perpendicular to the leading edge across most regions except the wing tip, and this characteristic

still holds under GE. This perspective effectively demonstrates the rationality of the velocity decomposition method for swept wings. Furthermore, the flow over both rectangular and swept wings can be fully decomposed into two components: one perpendicular and the other parallel to the leading edge.

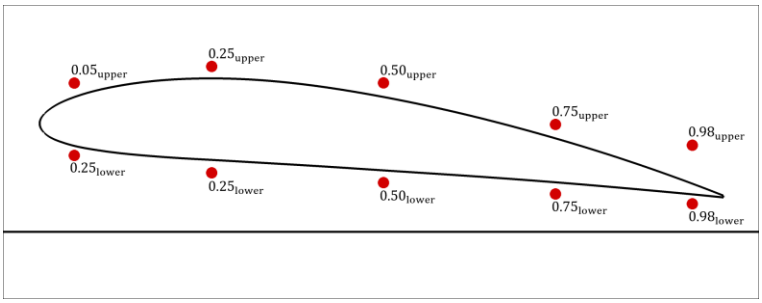


Figure 15 – Streamline sampling points.

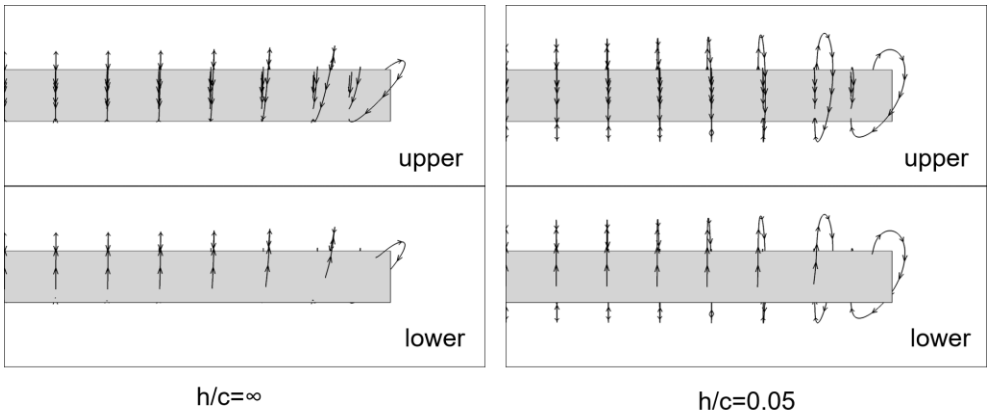


Figure 16 – Spatial streamlines passing through sampling points on upper and lower surfaces of rectangular wing with AR =15.

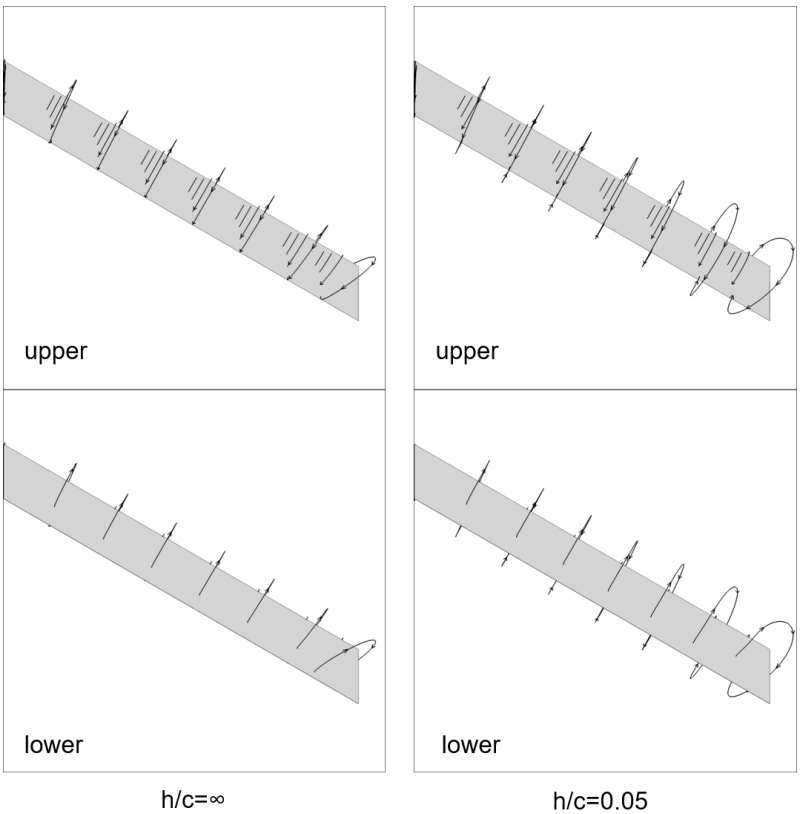


Figure 17 – Spatial streamlines passing through sampling points on upper and lower surfaces of 30°swept wing with AR =15 .

For convenience, the direction normal to the leading edge is defined as the **n**-direction, and the direction parallel to the leading edge as the **t**-direction. Figures 15 and 16 demonstrate that the dominant flow around the wing remains perpendicular to the leading edge, even at extremely low flight heights. Analysis of the t-direction flow follows.

For a swept wing with infinite AR, the oncoming flow in the present forward flight perspective can be intuitively decomposed into the n-direction and t-direction, as shown in Figure 18. The disturbance characteristics in the **n**-direction are consistent with those of an airfoil, where the airfoil corresponds to the wing section aligned parallel to the **n**-direction. In the **t**-direction, the flow velocity outside the boundary layer is uniform at all locations and equals $U_\infty \sin\Lambda$.

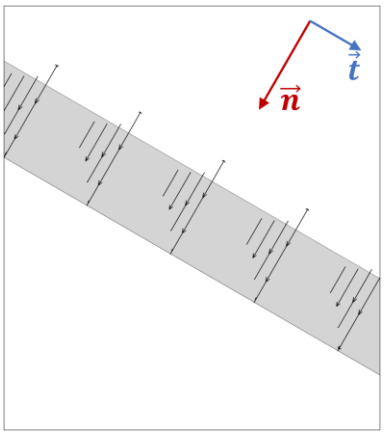


Figure 18 – Spatial streamlines passing through sampling points on upper surface of 30° swept wing with infinite AR at h/c = 0.05

For wings of finite span, disturbances at the wingtip induce variations in the **t**-direction velocity. Straight lines parallel to the **t**-direction are drawn across the sampling points, and the **t**-direction velocity along these lines is extracted for both the rectangular wing (0° swept) and the 30° swept wing with the same AR = 15 at different h/c. Figure 19 presents the results for sampling points on the upper surface, while Figure 20 corresponds to those on the lower surface. The development of wingtip flow over the wing surface is affected by sweep, which leads to magnitude differences in the **t**-direction velocity between the two configurations. Apart from the region near the symmetry plane of the swept wing, the **t**-direction velocity distributions follow highly consistent trends. This phenomenon is also observed under GE. This indicates that the **t**-direction flow characteristics of both wings are similar and primarily induced by wingtip flow.

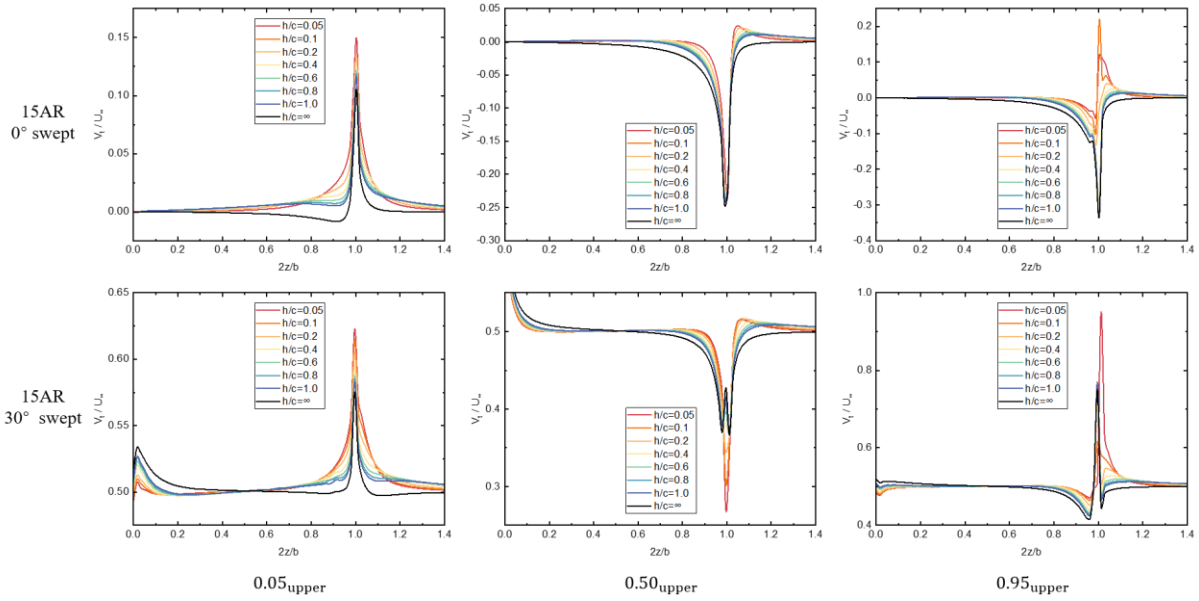


Figure 19 – **t**-direction velocity along lines through sampling points (upper surface).

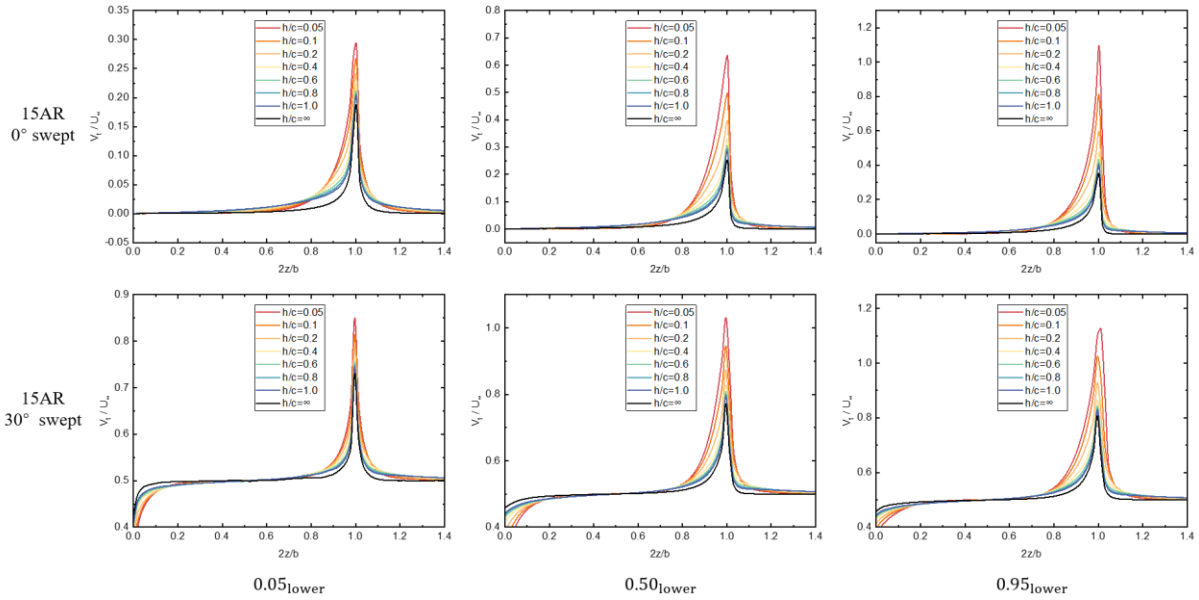


Figure 20 – **t**-direction velocity along lines through sampling points (lower surface).

3.4 Formation mechanism of 2D flow region

Based on the above discussion, the flow characteristics of rectangular and swept wings are essentially identical. The overall flow is a superposition of components normal and parallel to the leading edge, and this principle also holds under GE. Accordingly, the two configurations share the same flow mechanism for forming the uniform two-dimensional flow region in GE.

Figure 21 presents streamlines of the NACA 4412 airfoil at different flight heights under the forward flight frame. Intuitively, the moving airfoil propels the airflow within the gap between its lower surface and the ground. At very small flight heights, the flow velocity in this gap rises significantly and approaches the flight speed of the airfoil. When superimposing the free-stream flow back, the net velocity of the gap flow becomes considerably low. This phenomenon corresponds to the block effect widely adopted in conventional GE explanations, which indicates that airflow can hardly pass through the narrow gap at low flight heights.

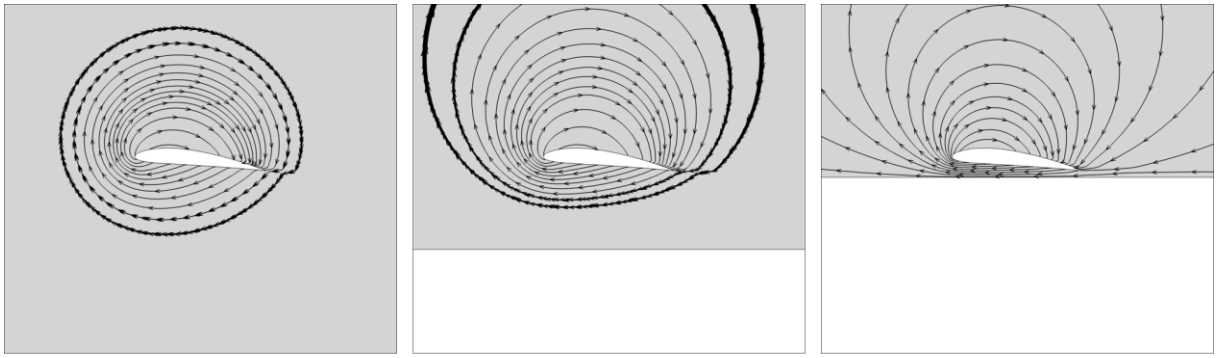


Figure 21 – Streamlines of the NACA 4412 airfoil at different flight heights under the forward flight frame.

The vortex image method is a classic approach for interpreting GE. To form a perfectly straight streamline representing the ground, treating the ground as a symmetry plane is the most straightforward solution. From the forward flight perspective, the flow disturbances around the airfoil clearly exhibit the characteristics induced by the bound vortex. Figure 22 illustrates the flow fields of the image bound vortex for GE and the image point vortex. The two flow patterns show excellent agreement, which is physically intuitive under the forward flight frame.

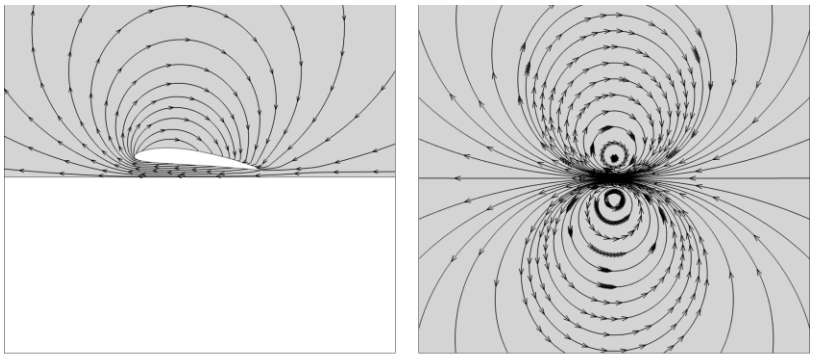


Figure 22 – Streamlines of the NACA 4412 airfoil under GE and image point vortex.

The 2D flow region formed on the inboard wing section arises because flow disturbances from the wing tip cannot propagate inward. In other words, the induced effects of free vortices and wingtip vortices fail to penetrate this region.

Figure 23 compares the spatial streamlines passing through identical sampling points on the NACA 4412 airfoil (AR = ∞) and different sections of the rectangular wing with AR =15 in an unbounded flow field. For the two-dimensional airfoil, streamlines always close at the trailing edge. Near the wing tip (2z/b = 0.8), streamlines evolve into spiral shapes due to the transport of spanwise velocity, and only a segment of this streamline is presented here. From the airfoil, across the symmetry plane of the rectangular wing to the wing tip, streamlines expand toward the leading edge, which is accompanied by a reduction in the vorticity enclosed by the streamlines.

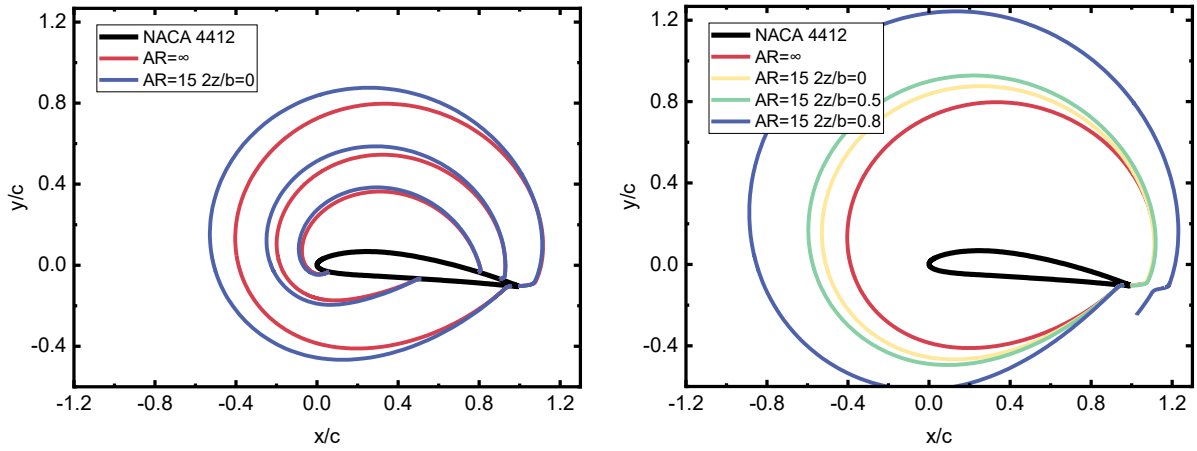


Figure 23 – Spatial streamlines passing through identical sampling points on the NACA 4412 airfoil (AR = ∞) and different sections of the rectangular wing with AR =15 in an unbounded flow field.

Intuitively, the presence of the ground boundary suppresses such streamline deflection and expansion. Consequently, the flow over a substantial portion of the wing span is confined and behaves identically to that of a two-dimensional airfoil, as illustrated in Figure 24.

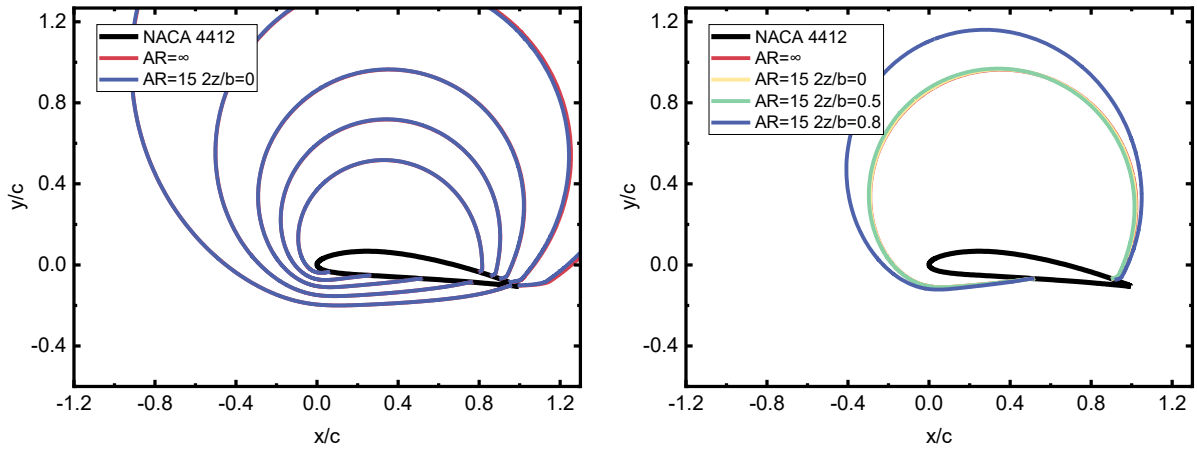


Figure 24 – Spatial streamlines passing through identical sampling points on the NACA 4412 airfoil (AR = ∞) and different sections of the rectangular wing with AR =15 at h/c =0.05.

4. Conclusion

This paper investigates the static ground effect of high-aspect-ratio wings. From the perspective of forward flight, comparative analyses are conducted on rectangular and swept wings. The main conclusions are summarized as follows:

1. The flow fields over rectangular and swept wings share essentially the same characteristics, which are formed by the superposition of airfoil disturbances normal to the leading edge and flow components parallel to the leading edge.
2. Under ground effect, the influence range of wingtip flow is limited and nearly constant. Such disturbances cannot propagate to the inboard wing section, where a two-dimensional flow region is consequently formed.
3. The two-dimensional flow in the inboard region is primarily attributed to the constraint of the ground boundary, which suppresses streamline deflection and divergence. Flow escapes from the wingtip only in the tip region, accompanied by a reduction of the bound vortex strength.

5. Contact Author Email Address

Corresponding author: Qiulin Qu

Email: qql@buaa.edu.cn

6. Copyright Statement

The authors confirm that they, and/or their company or organization, hold copyright on all of the original material included in this paper. The authors also confirm that they have obtained permission, from the copyright holder of any third-party material included in this paper, to publish it as part of their paper. The authors confirm that they give permission, or have obtained permission from the copyright holder of this paper, for the publication and distribution of this paper as part of the ICAS proceedings or as individual off-prints from the proceedings.

References

[1] Droney C, Harrison N and G. Gatlin. Subsonic ultra-green aircraft research: Transonic truss-braced wing technical maturation. *Proceedings of the 31st Congress of the International Council of the Aeronautical Sciences*, Belo Horizon, Brazil, pp 9-14. 2018.

[2] Harrison N, Gatlin G, Viken S, Beyar M, Dickey E, Hoffman K and Reichenbach E. Development of an efficient M=0.80 transonic truss-braced wing aircraft. *AIAA Scitech 2020 Forum*, Orlando, FL, AIAA 2020-0011, 2020.

[3] Hiemcke, C. NACA 5312 in ground effect-wind tunnel and panel code studies. *15th Applied Aerodynamics Conference*, Atlanta, Georgia, pp 1997-2320, 1997.

[4] Tremblay-Dionne V, and Lee T. Discrepancy in the aerodynamic property and flowfield of a symmetric airfoil produced by the stationary and moving ground effect. *Journal of Fluids Engineering*, Vol. 143, No. 2, Paper 021301, 2021.

[5] Ahmed M, Takasaki T and Kohama Y. Aerodynamics of a NACA4412 airfoil in ground effect. *AIAA Journal*, Vol. 45, No.1, pp 37-47, 2007.

[6] Qu Q, Wang W, Liu P and Agarwal R. Airfoil aerodynamics in ground effect for wide range of angles of attack. *AIAA Journal*, Vol. 53, No. 4, pp 1048-1061, 2015.

[7] Shi X, Qu Q, Liu P, Xun Y, Bu C and Chen H. Feasibility analysis of fixed plates in chord-dominated static ground effect wind-tunnel experiment. *AIAA Journal*, Vol. 60, No. 9, pp. 5286-5298, 2022.

[8] Harvey J and Perry F. Flowfield produced by trailing vortices in the vicinity of the ground. *AIAA Journal*, Vol. 9, No. 8, pp 1659-1660, 1971.

[9] Ciffone D and Pedley B. Measured wake-vortex characteristics of aircraft in ground effect. *AIAA Journal*, Vol. 16, No. 2, pp 102-109, 1979.

[10] Han C and Cho J. Unsteady trailing vortex evolution behind a wing in ground effect. *Journal of Aircraft*, Vol. 42, No. 2, pp 429-434, 2005.

[11] Lu A, Tremblay-Dionne V and Lee T. Experimental study of aerodynamics and wingtip vortex of a rectangular wing in flat ground effect. *The ASME Journal of Fluids Engineering*, Vol.141, No. 11, Paper 111108, 2019.

[12] Tan C. Lifting-line solution for a symmetrical thin wing in ground effect. *AIAA Journal*, Vol. 24, No. 7, pp 1193-1194, 1986.

[13] Zong Z, Liang H and Zhou L. Lifting line theory for wing-in-ground effect in proximity to a free surface. *Journal of Engineering Mathematics*, Vol. 74, pp 143–158, 2011.

[14] Valenzuela J and Takahashi T. Wing design strategies for vehicles designed to operate in ground effect. *AIAA SCITECH 2024 Forum*, Orlando, Florida, AIAA 2024-0003, 2024.

[15] Phillips W and Hunsaker D. Lifting-line predictions for induced drag and lift in ground effect. *Journal of Aircraft*, Vol. 50, No.4, pp 1226-1233, 2013.

[16] Wieselsberger C. Wing resistance near the ground. 1922.

[17] Guermond J. A generalized lifting-line theory for curved and swept wings. *Journal of Fluid Mechanics*, Vol.211, pp 497-513, 1990.

[18] Phillips W and Snyder D. Modern adaptation of Prandtl's classic lifting-line theory. *Journal of Aircraft*, Vol. 37, No. 4, pp.662-670, 2000.

[19] Zerihan J and Zhang X. Aerodynamics of a single element wing in ground effect. *Journal of Aircraft*, Vol. 37, No. 6, pp 1058-1064, 2000.